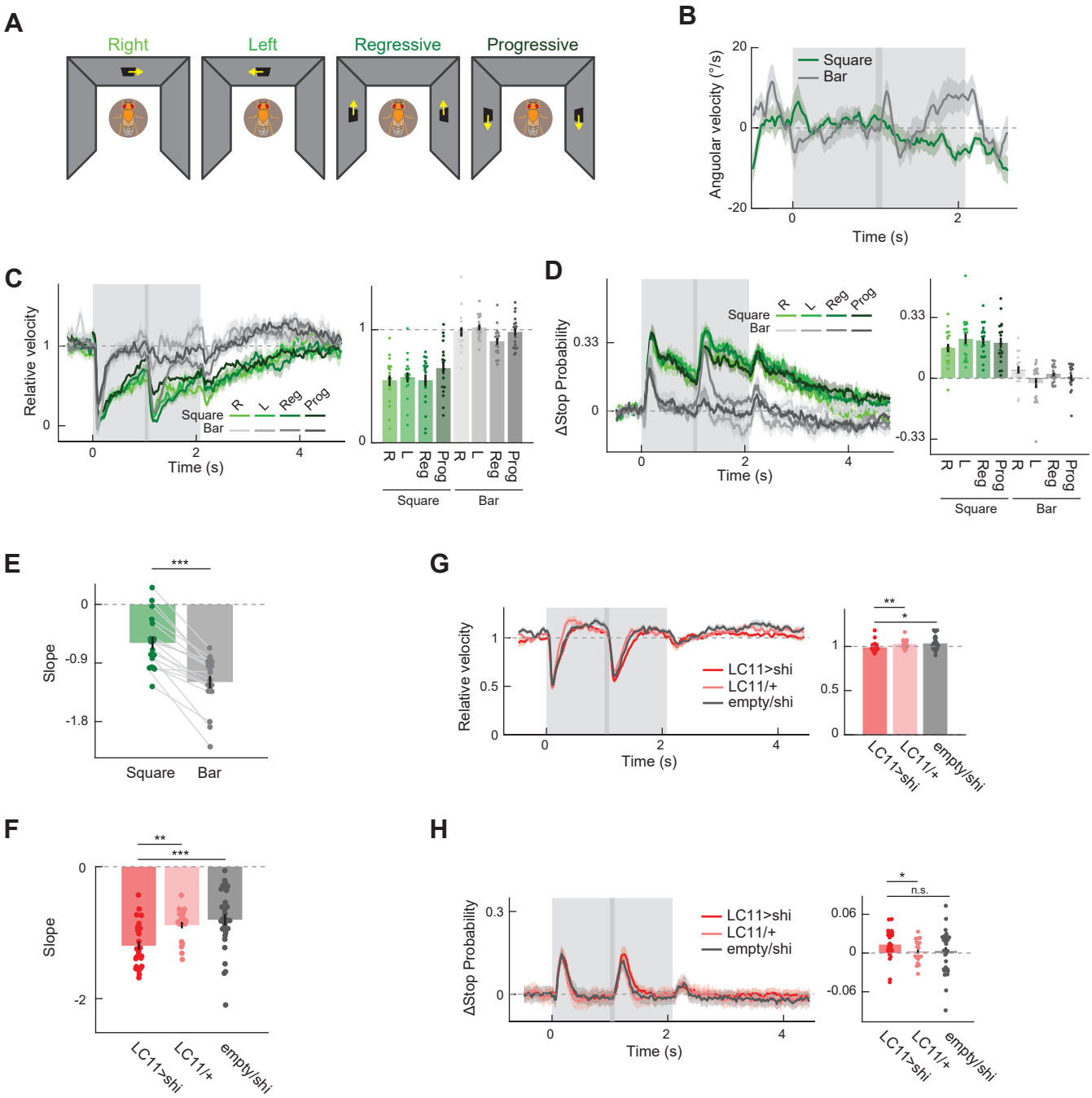
A
Right
Left
Regressive
Progressive
B
Square
Bar
Angular velocity (°/s)
Time (s)
C
Relative velocity
Square
Bar
R
L
Reg
Prog
Time (s)
D
ΔStop Probability
Time (s)
E
Slope
Square
Bar
***
F
Slope
**
***
LC11>shi
LC11/+
empty/shi
G
Relative velocity
LC11>shi
LC11/+
empty/shi
Time (s)
**
*
H
ΔStop Probability
LC11>shi
LC11/+
empty/shi
Time (s)
*
n.s.

Figure S1. Detailed characterization of flies' walking response to small objects, Related to Figures 1, 2.

(A) The four configurations of the visual stimuli. Squares or bars appeared either in front of or to the sides of the fly. Objects at the front moved either right or left, and objects at the sides moved either regressively or progressively. (B) Turning responses of flies to objects presented in front. Positive turning indicates turning in the same direction as the movement of the object. (C, D) (*left*) Average relative walking speed (C) or change in instantaneous stop probability (D) by object type and stimulus configuration. The gray shaded region corresponds to the period during which stimuli were presented, and the area with a darker shade indicates when the stimuli were moving. (*right*) Relative walking speed (C) and change in instantaneous stop probability (D), averaged over 4 seconds after the stimulus onset. The four stimulus configurations triggered qualitatively similar behaviors within each object type. A notable exception is the regressively moving bars, which triggered more slowing responses than other configurations of bars, consistently with previous reports of regressive-selective slowing in *Drosophila* [S1,S2]. (E) Slope of the linear functions fit to individual flies' log-log histograms of stop duration initiated by the movement of objects. (F) Slope of the linear functions fit to log-log histogram of stop duration initiated by the movement of small squares in LC11-silenced flies and corresponding control genotypes. (G, H) (*left*) Average relative walking velocity (G) and change in instantaneous stop probability (H) in response to the presentation of bars in LC11-silenced flies and corresponding control flies. (*right*) Time-averaged relative velocity (G) and change in instantaneous stop probability (H) in response to the presentation of bars, in LC11-silenced and control flies. Averaged over 4 seconds after the stimulus onset. (B – E) N = 18 flies. (F - H) n = 25 flies (LC11/shi), 18 (LC11/+), 30 (empty/shi). n.s. non-significant ($p > 0.05$); * $p<0.05$; ** $p<0.01$; *** $p < 0.001$; **** $p<0.0001$ in Wilcoxon sign-rank (E) or rank-sum (F-H) test.

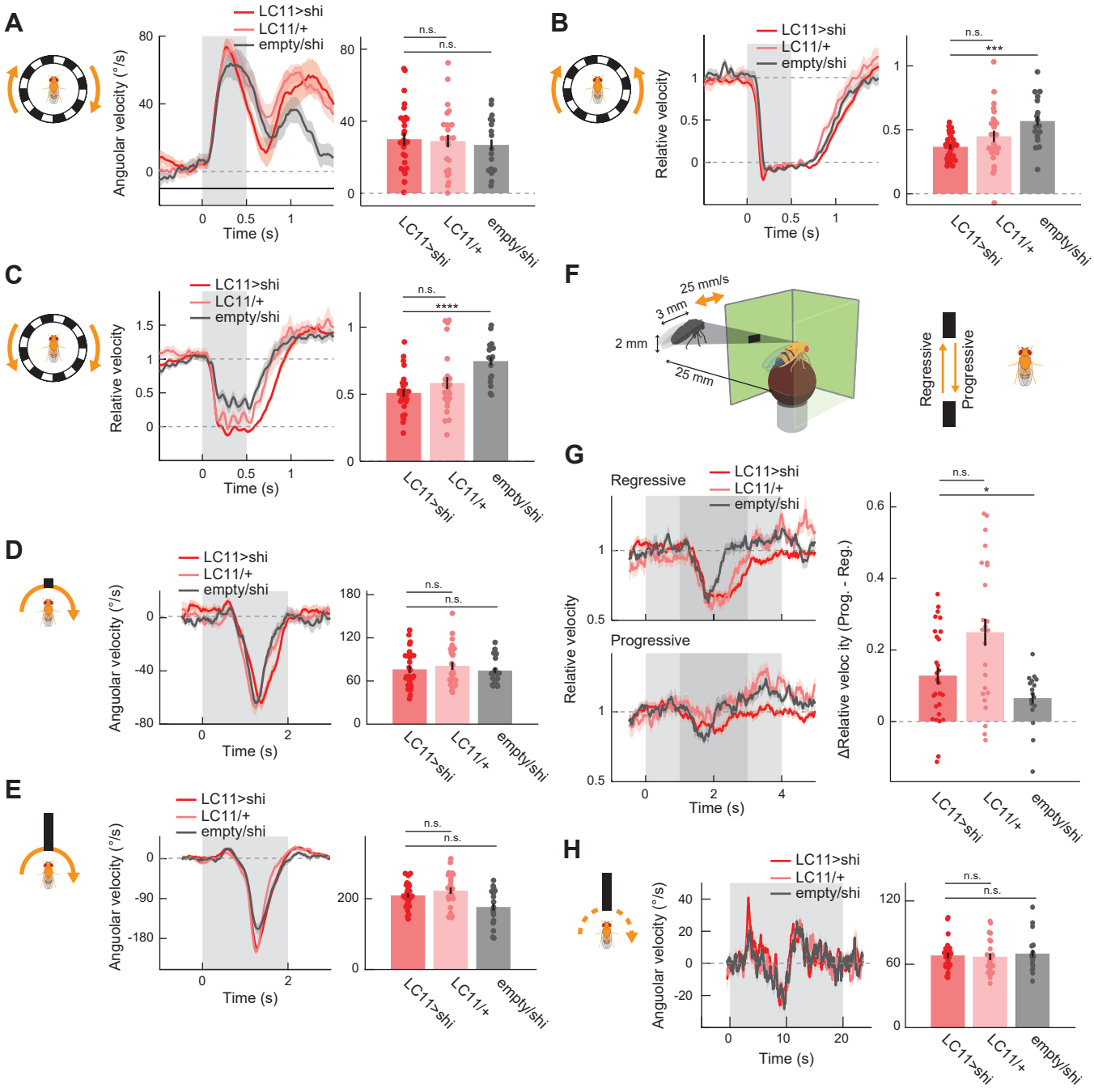
A
LC11>shi
LC11/+
empty/shi
Angular velocity (°/s)
Time (s)
n.s.
n.s.
B
Relative velocity
***
C
****
D
E
F
25 mm/s
3 mm
2 mm
25 mm
Regressive
Progressive
G
Regressive
Progressive
ΔRelative veloc ity (Prog. - Reg.)
*
H

Figure S2. Specificity of the effects of LC11 silencing, Related to Figure 2.

In none of the behaviors we examined except small object-induced stopping did LC11-silenced flies show significant differences from both Gal4 and UAS control flies. (A) (*left*) Optomotor turning responses of flies to drifting sinusoidal gratings in LC11-silenced and control flies [S3]. Positive turning indicates turning in the same direction as the stimulus. (*right*) Turning responses in LC11-silenced and control flies, averaged over 1/4 second after the stimulus onset. (B, C) (*left*) Relative walking velocity of LC11-silenced and control flies in response to regressive (B) or progressive (C), translational sinusoidal gratings. Flies slowed in response to translational optic flow, as previously reported [S1]. (*right*) Relative velocity of LC11-silenced and control flies in response to regressive (B) or progressive (C) gratings, averaged over 1/4 second after the stimulus onset. (D, E) (*left*) Aversive turning responses of LC11-silenced and control flies in response to either a 5º x 5º black square or a 5º x 106º black bar rotated around the fly at 180º/s, starting and ending directly behind the fly [S4]. (*right*) Maximum absolute aversive turning velocity of LC11-silenced and control flies in response to (D) a square or (E) a bar. (F) A schematic of the "fly-mimic" stimulus. An approximately fly-sized (3 mm wide, 2mm tall) rectangular black object moved parallel to the fly either regressively or progressively at 25 mm/s. The distance between the fly and the trajectory of the object was 25 mm, so that the object occupied ~6.8° by ~4.6° of visual space. (G) Relative walking velocity of LC11-silenced and control flies in response to either (*top left*) regressive or (*bottom left*) progressive fly-mimic stimuli. The gray shaded region indicates the period during which the fly-mimic object was presented, and the darker shade of gray indicates when the object was moving. (*right*) Difference between time-averaged relative velocity of LC11-silenced and control flies in response to progressive and regressive fly-mimic objects. The temporal averaging window was between 1 and 3 s after stimulus onset. The all genotypes showed significantly more slowing in response to regressive stimuli (LC11>shi: $p<0.0001$; LC11/+: $p<0.0001$; empty/shi: $p<0.01$; Wilcoxon sign-rank test) [S2]. (H) (*left*) Fixative turning response of LC11-silenced and control flies in response to a 10º x 106º black bar slowly rotated around the fly at 18º/s [S5]. (*right*) Maximum absolute fixative turning velocity of LC11-silenced and control flies in response to a bar. n = 28 flies (LC11/shi), 24 (LC11/+), 17 (empty/shi). * $p<0.05$; ** $p<0.01$; *** $p < 0.001$; **** $p<0.0001$ in Wilcoxon rank-sum test.

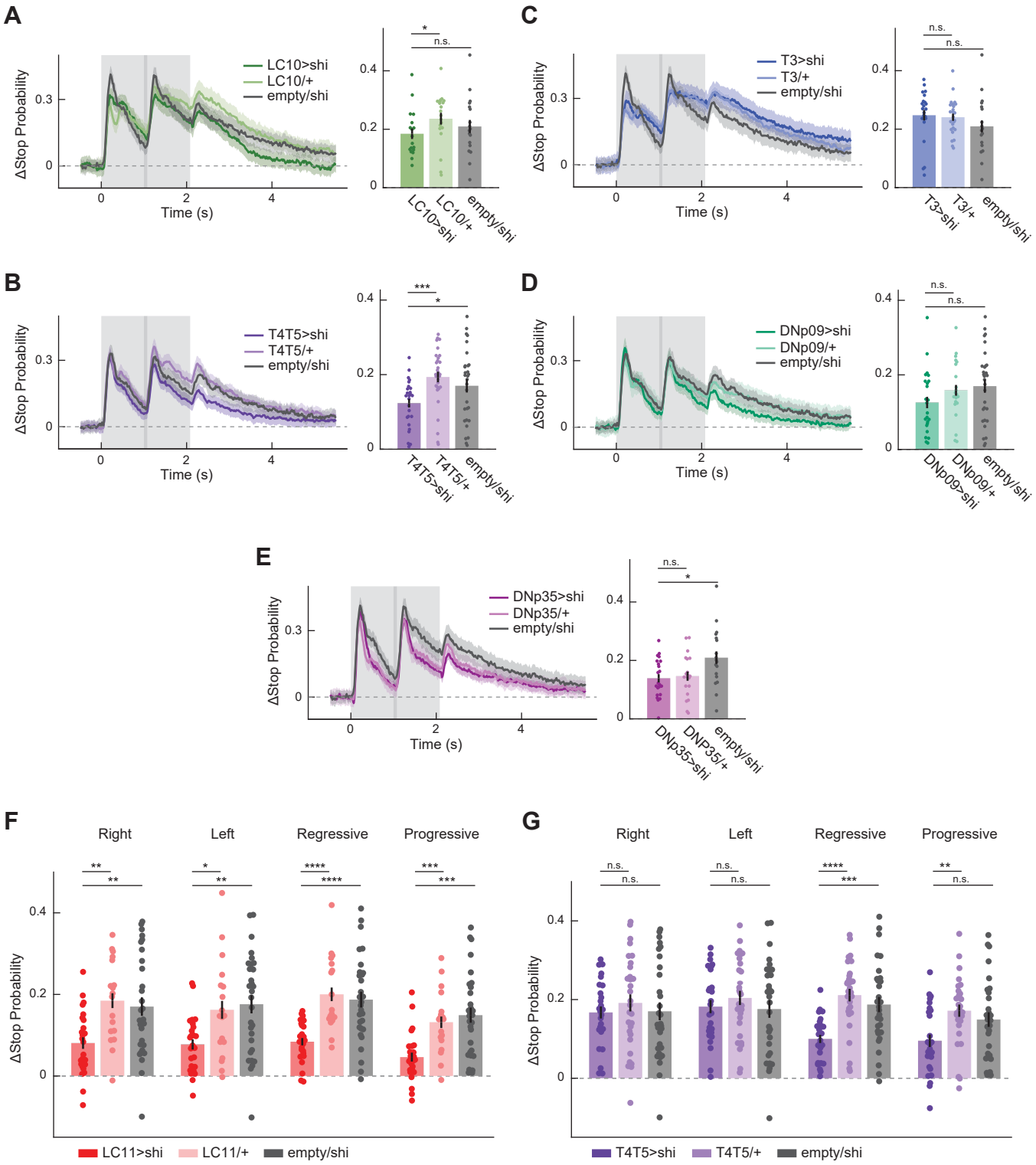
A
ΔStop Probability
LC10>shi
LC10/+
empty/shi
Time (s)
*
n.s.
LC10>shi
LC10/+
empty/shi
B
T4T5>shi
T4T5/+
empty/shi
***
*
C
T3>shi
T3/+
empty/shi
n.s.
D
DNp09>shi
DNp09/+
E
DNp35>shi
DNp35/+
F
Right
Left
Regressive
Progressive
LC11>shi
LC11/+
G
T4T5>shi
T4T5/+

Figure S3. Effect of silencing various neurons on object-induced freezing, Related to Figure 2.

(A - E) Change in instantaneous stop probability in response to small square stimuli shown in **Figure 1B**, in LC10-silenced (A), T4T5-silenced (B), T3-silenced (C), DNp09-silenced (D), and DNp35-silenced (E) flies with corresponding Gal4 and UAS controls, either against time (*left*) or averaged over time (*right*). The temporal averaging window was between 0 and 4 s after the onset of the stimulus. (F, G) Time-averaged change in instantaneous stop probability in response to small square stimuli shown in **Figure 1B** in LC11-silenced (F) and T4T5-silenced (G) flies, by the position and direction of motion (see **Figure S1A**). While silencing of LC11 reduced slowing significantly regardless of object position or motion direction, T4T5 silencing did so only when stimuli appeared on the side of the flies, implying a parallel, T4T5-dependent mechanism of object-induced stopping. (A) n = 18 flies (LC10/shi), 20 (LC10/+), 18 (empty/shi). (B, G) n = 26 flies (T4T5/shi), 30 (T4T5/+), 30 (empty/shi). (C) n = 22 flies (T3/shi), 25 (T3/+), 18 (empty/shi). (D) n = 24 flies (DNp09/shi), 21 (DNp09/+), 30 (empty/shi). (E) n = 22 flies (DNp35/shi), 20 (DNp35/+), 18 (empty/shi). (F) n = 25 flies (LC11/shi), 18 (LC11/+), 30 (empty/shi). n.s. non-significant ($p > 0.05$); * $p<0.05$; ** $p<0.01$; *** $p < 0.001$; **** $p<0.0001$ in Wilcoxon sing-rank test.

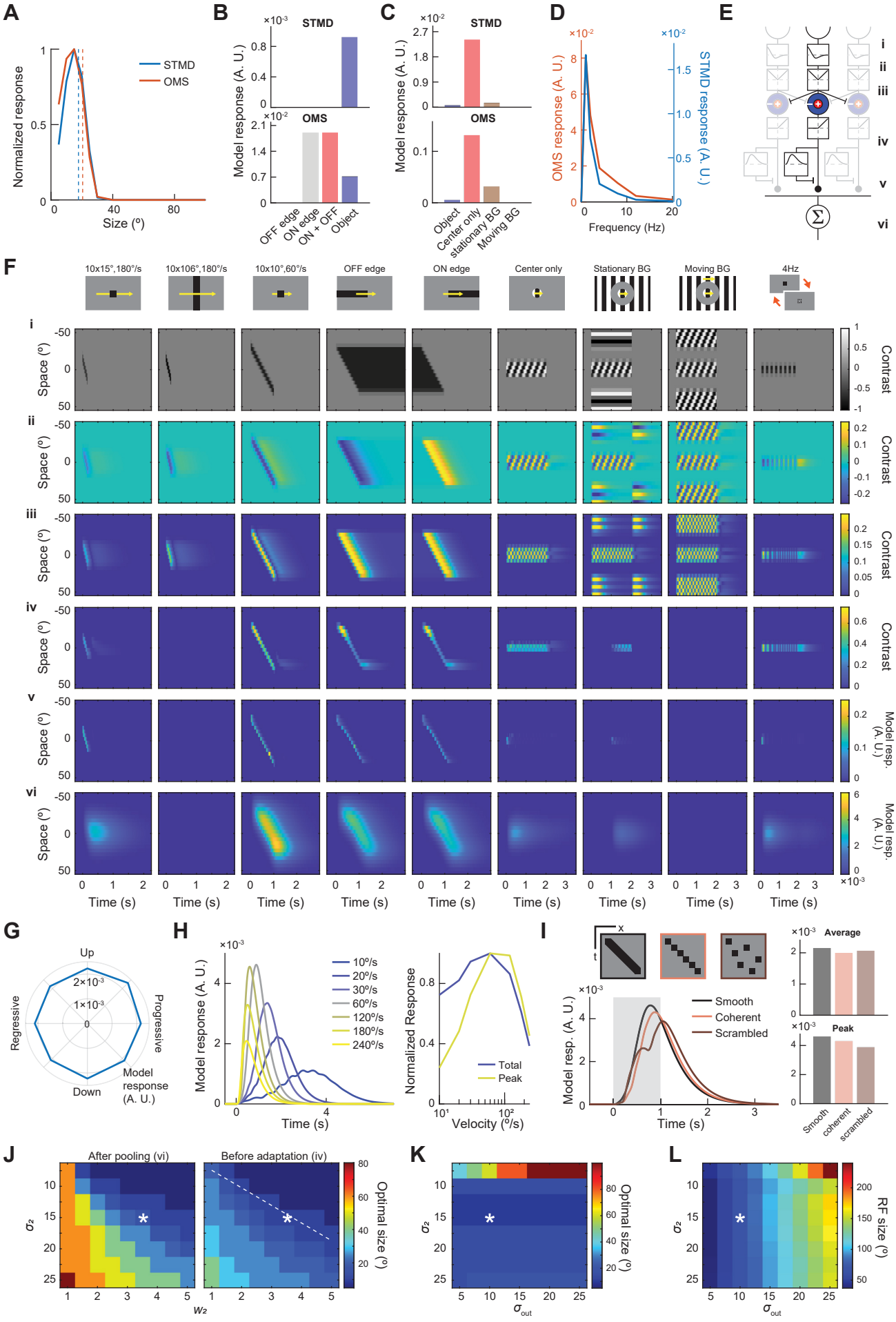
A
Normalized response
STMD
OMS
Size (°)
B
STMD
OMS
Model response (A. U.)
OFF edge
ON edge
ON + OFF
Object
C
STMD
OMS
Model response (A. U.)
Object
Center only
stationary BG
Moving BG
D
OMS response (A. U.)
STMD response (A. U.)
Frequency (Hz)
E
i
ii
iii
iv
v
vi
F
10x15°,180°/s
10x106°,180°/s
10x10°,60°/s
OFF edge
ON edge
Center only
Stationary BG
Moving BG
4Hz
Space (°)
Contrast
Model resp. (A. U.)
Time (s)
G
Up
Progressive
Down
Regressive
Model response (A. U.)
H
Model response (A. U.)
Time (s)
10°/s
20°/s
30°/s
60°/s
120°/s
180°/s
240°/s
Normalized Response
Total
Peak
Velocity (°/s)
I
Model resp. (A. U.)
Smooth
Coherent
Scrambled
Time (s)
Average
Peak
J
After pooling (vi)
Before adaptation (iv)
Optimal size (°)
K
Optimal size (°)
L
RF size (°)

Figure S4. Detailed characterization of the models, Related to Figure 4.

(A-D) Responses of STMD and OMS models (see **STAR Methods**) to stimuli used in **Figure 3, 4**. (A) The size tuning curves, as in **Figure 4G**. The RF sizes of the two models, indicated by dotted vertical lines, approximately match their optimal object sizes. Note that the parameters of the two alternative models were determined such that they prefer 15º objects, similar to the DD model shown in **Figure 4**. (B) Responses of the STMD (*top*) and OMS (*bottom*) models to the decoupled edge stimuli (**Figures 3I, 4I**). The STMD model does not respond to decoupled edges due to multiplicative interaction between ON and OFF channels, while the OMS model responds to ON edges. (C) Responses of the STMD (*top*) and OMS (*bottom*) models to localized grating stimuli (**Figures 3L, 4K**). The background stimuli suppress the responses of the both models. The both models prefer sustained local motion to translating objects. (D) Flicker frequency-tuning curves of the two alternative models, as in **Figures 3M, 4N**. The both models are more tightly tuned to particular temporal frequency. Their integrated responses to repetitive flickers are also greater than their responses to translating objects (see B, C). (E) A schematic of the DD model, redrawn from **Figures 4A**. Roman numerals indicate the steps visualized in each row of (F). (F) Step-by-step snapshots of how different stimuli are transformed at each stage of the model. Columns correspond to different stimuli, and rows correspond to different point in the model, as indicated by roman numerals in (E). Each space-time plot shows responses of a horizontal array of model units corresponding to the visual equator. The stimuli shown here are, from left to right, (1) a 10º x 15º black object moving at 180º/s (**Figure 4F**), (2) a 10º x 106º black bar moving at 180º/s (**Figure 4F**), (3) a 10º x 10º black square moving at 60º/s (**Figure 4H, J**), (4) a 10º wide decoupled OFF edge moving at 60º/s (**Figure 4H**), (5) a 10º wide decoupled ON edge moving at 60º/s (**Figure 4H**), (6) a square wave grating with $\lambda = 20º$, moving at 60º/s and localized in an aperture with 20º diameter (**Figure 4J**), (7) the localized grating with a stationary background, (8) the localized grating with a moving background, and (9) a single black square flickering at 4Hz (**Figure 4L**). (G) Directional tuning of the DD model, measured as time-averaged response of the model to 10º x 10º black squares moving in eight different directions at 60º/s. (H) (*left*) Responses of the DD model to a 10º x 10º black square moving at various velocities. The lengths of the trajectories were kept constant at 60º. The model responded to objects with a wide range of velocities [S6]. (*right*) Velocity tuning curves of the DD model, either based on time-integrated (blue) or peak (yellow) response to the squares with different velocities. (I) (*left*) Responses of the DD model to a smoothly translating 10º x 10º square or velocity matched apparent motion stimuli, either coherent or scrambled (schematics of the stimuli are on *top left*). (*right*) Time-averaged (*top*) or peak (*bottom*) model responses to a smoothly moving object or apparent motion stimuli. Overall, the model did not show strong preference to coherence of motion, while the peak responses were marginally larger for coherent stimuli over scrambled ones. This is because coherent stimuli, but not scrambled ones, hit most strongly connected central input units in immediate succession, similar to mechanisms previously suggested in vertebrate retina [S7]. (J-L) Dependence of optimal object sizes (J, K) and RF sizes (L) on spatial parameters in the DD model. The parameters used in **Figure 4** are indicated with white asterisks. (J) Optimal object sizes of the pooling units (*left*, vi in E) and input units before adaptation (*right*, iv in E), as a function of w_2 and σ_2 (see **STAR Methods**), probed with the stimuli in **Figure 4F**. w_1 and σ_1 were fixed at 1º and 5º, respectively. The optimal sizes of the model output were larger than those of input units for broad range of parameters. When the inhibitory lobe of the spatial filter is too shallow, namely when w_2 is too small, the model loses its selectivity for small sizes even when input units are still tuned to sizes less than 20º. Optimal object sizes (K) and RF sizes (L), as a function of σ_2 and σ_{out} (see **STAR Methods**). The parameter w_2 was linearly scaled with σ_2 according to the white dotted line in (J), in order to give 10º size tuning at the input level. Size tuning did not depend strongly on σ_{out}, and the RF size increased as σ_{out} increased, without obvious interaction.

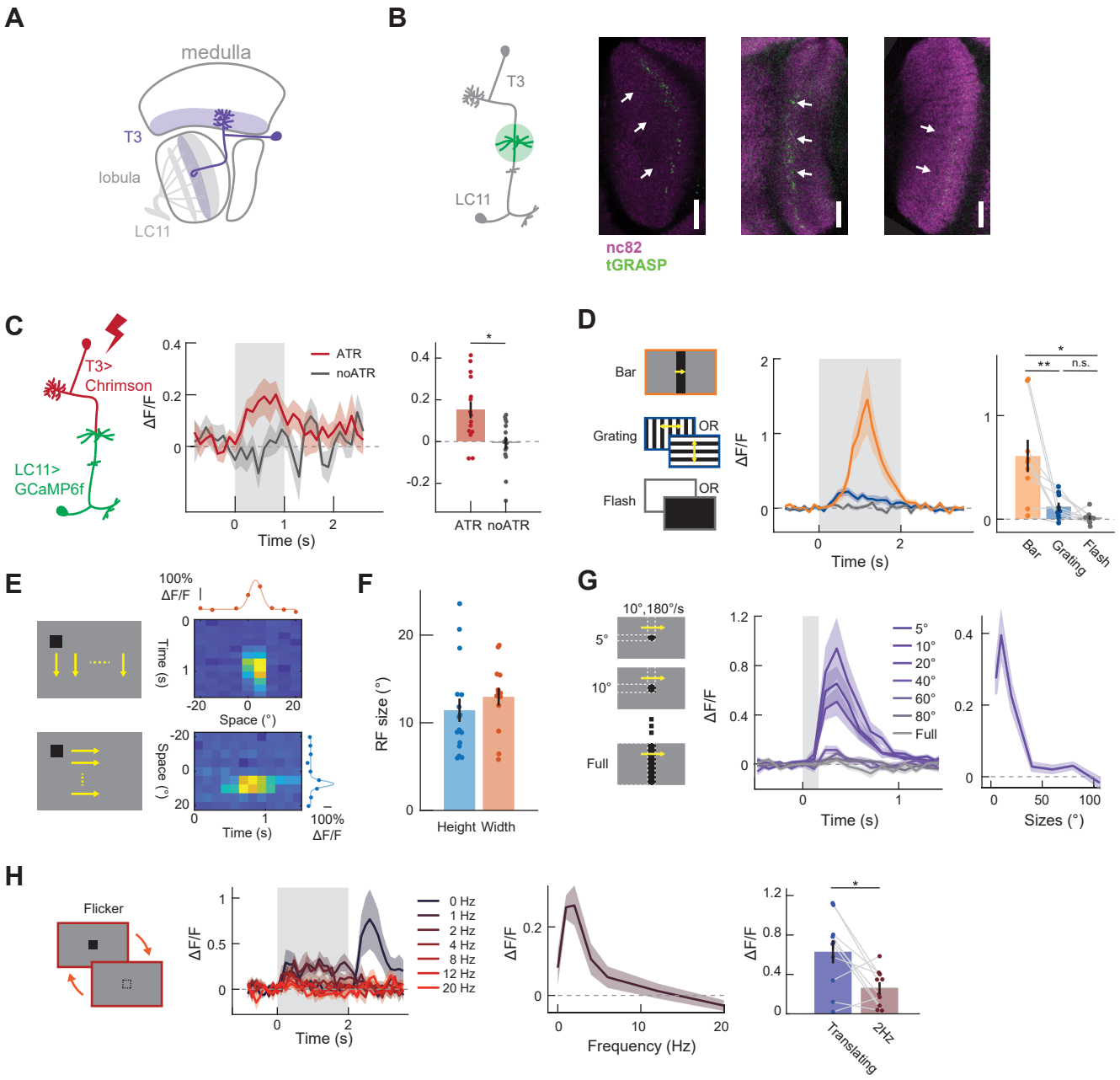
A
medulla
T3
lobula
LC11
B
T3
LC11
nc82
tGRASP
C
T3>
Chrimson
LC11>
GCaMP6f
ATR
noATR
ΔF/F
Time (s)
ATR noATR
D
Bar
Grating
OR
Flash
OR
ΔF/F
Time (s)
n.s.
Bar
Grating
Flash
E
100%
ΔF/F
Time (s)
Space (°)
Space (°)
Time (s)
100%
ΔF/F
F
RF size (°)
Height Width
G
10°,180°/s
5°
10°
Full
ΔF/F
Time (s)
5°
10°
20°
40°
60°
80°
Full
Sizes (°)
H
Flicker
ΔF/F
Time (s)
0 Hz
1 Hz
2 Hz
4 Hz
8 Hz
12 Hz
20 Hz
ΔF/F
Frequency (Hz)
ΔF/F
Translating
2Hz

Figure S5. Characterization of T3, a putative excitatory input to LC11, Related to Figure 4.

(A) The anatomy of T3 neurons. T3 neurons have putative dendrites in deep medulla and axon terminals in Lo3 (see **Figures 4B, S7C-I**). (B) Fluorescent labeling of T3-LC11 synapse by tGRASP. White arrows indicate labeled synapses in Lo3. Scale bars indicate 20 μm. (C) (*left*) Average calcium response of LC11 neurons when T3 neurons were optogenetically activated with Chrimson, with or without retinal feeding. (*right*) Responses of LC11 to optogenetic activation of T3 averaged over 1 s of stimulation, with or without retinal. Note that male flies were used in this particular experiment for the relative ease of generating blind male flies rather than females, under the assumption that T3-LC11 connectivity is not sex specific. (D) (*left*) Average calcium response of T3 neurons to the battery of full-field stimuli, as used in **Figure 5**. (*right*) Time-averaged responses of T3 to the battery of stimuli. Temporal averaging windows were 0 to 1.5 s for bars and 0 to 2 s for the other stimuli. (E) The RF of a typical individual T3 neuron, mapped with a single, translating square at various azimuths and elevations, as in **Figure 3C**. (F) The size of T3 RFs, measured as FWQM of Gaussian function fit to the spatial tuning curves of calcium responses. (G) (*left*) Average calcium responses of T3 to translating objects with various sizes. (*right*) The size tuning curve of T3 neurons. Responses were averaged within 0 to 1 s after the onset of the stimuli. The optimal object size of T3 approximately matched its RF size. (H) (*left*) Average responses of T3 neurons to a stationary square flickering at various temporal frequencies. (*middle*) Flicker frequency tuning curve of T3. Responses were averaged over 0 to 2 s after the onset of the stimuli. (*right*) Comparison of responses of T3 to a translating or 2Hz-flickering square. (D) n = 9 flies. (F) n = 16, 13 cells for vertical and horizontal spatial tuning curves, respectively. (G, H) n = 10 cells. n.s. non-significant; * $p<0.05$; ** $p<0.01$ in Wilcoxon rank-sum (C) or sign-rank (F, H) test.

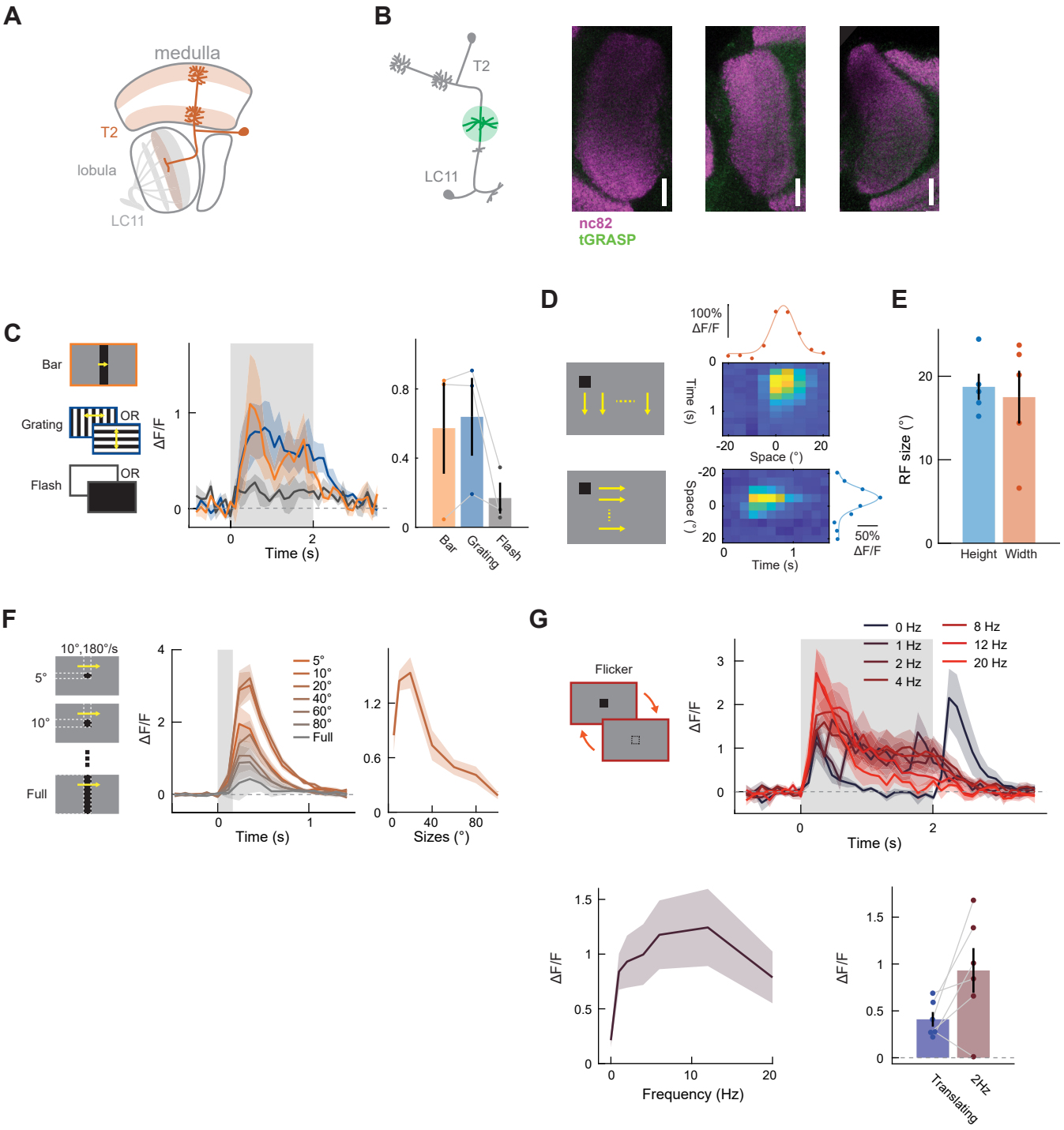
A
medulla
T2
lobula
LC11
B
T2
LC11
nc82
tGRASP
C
Bar
Grating
OR
Flash
OR
ΔF/F
Time (s)
Bar
Grating
Flash
D
100%
ΔF/F
Time (s)
Space (°)
50%
ΔF/F
E
RF size (°)
Height
Width
F
10°,180°/s
5°
10°
Full
ΔF/F
Time (s)
5°
10°
20°
40°
60°
80°
Full
Sizes (°)
G
Flicker
0 Hz
1 Hz
2 Hz
4 Hz
8 Hz
12 Hz
20 Hz
ΔF/F
Time (s)
ΔF/F
Frequency (Hz)
ΔF/F
Translating
2Hz

Figure S6. Characterization of T2, a putative excitatory input to LC11, Related to Figure 4.

(A) The morphology of T2. T2 has bistratified dendrites in medulla, and sends an axon to Lo2 (see **Figure 4C, S7C-I**). (B) Fluorescent labeling of T2-LC11 synapse by tGRASP. Synapses from T2 to LC11 were not detected by tGRASP. Scale bars indicate 20 μm. (C) T2's response to the battery of full-field stimuli, measured with jGCaMP7b. jGCaMP7b was used instead of GCaMP6f, because of weak expression of the driver line (R88C02-Gal4) [S8]. Compared to T3, T2 responded more to full field gratings and flashes relative to translating bars. The temporal averaging window was 0 to 1.5 s for bars and 0 to 2 s for the others. (D) A typical RF of a single T2 axon terminal, mapped in the same way as in **Figure 3C**. The following calcium imaging experiments used lexAop2-GCaMP6f with an amplifier construct, UAS-LexA, to compensate for weak expression level of the T2 driver. (E) RF sizes of individual T2 ROIs, measured as FWQM of Gaussian functions fit to vertical and horizontal tuning curves. (F) (*left*) Average calcium responses of T2 neurons to translating objects with different sizes. (*right*) Size tuning curve of T2 neurons. The optimal size of T2 approximately matched its excitatory RF size, similar to T3 neurons. The temporal averaging window was 0 to 1 s. (G) Responses of T2 neurons to flickering squares with various temporal frequencies over time (*top*) or time-averaged between 0 to 2 s after the stimulus onset (*bottom left*). T2 neurons responded strongly to flickers at various temporal frequencies, but adapted to those stimuli, especially at higher temporal frequencies. Temporal frequency tuning curve of T2 differed from those of LC11 and T3 in that it peaked at about 10Hz. (*bottom right*) The time-averaged response of T2 to 2Hz flicker appeared to be smaller than its response to translating squares, unlike in T3 or LC11 (*right*). (C) n = 3 flies. (E) n = 5 cells (vertical), 5 (horizontal). (F, G) n = 6 cells.

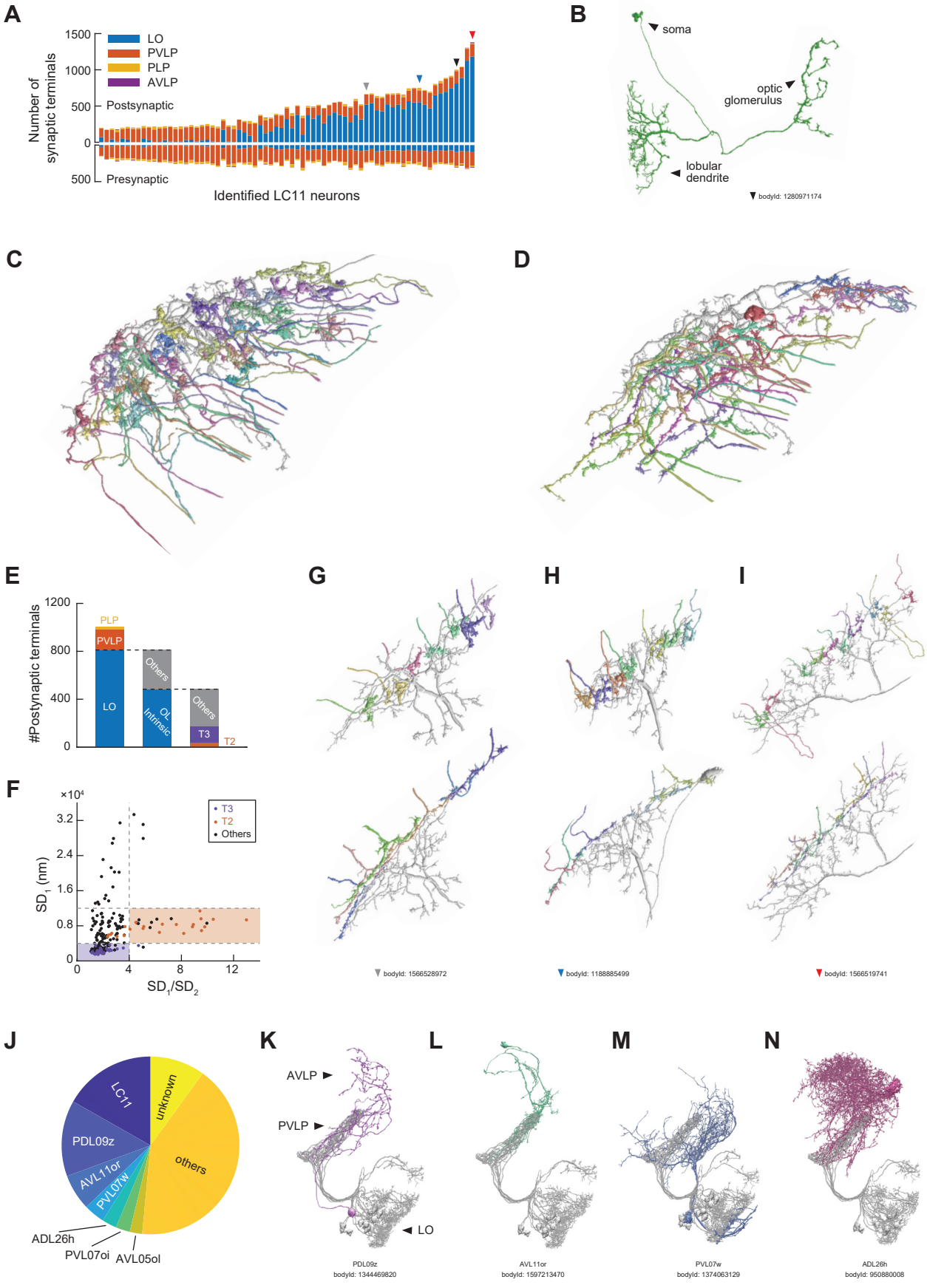
A
1500
1000
500
0
500
LO
PVLP
PLP
AVLP
Postsynaptic
Presynaptic
Number of synaptic terminals
Identified LC11 neurons
B
soma
optic glomerulus
lobular dendrite
bodyId: 1280971174
C
D
E
1200
800
400
0
#Postsynaptic terminals
PLP
PVLP
LO
Others
Others
T3
T2
F
×10⁴
3.2
2.4
1.6
0.8
0
0
4
8
12
SD1 (nm)
SD1/SD2
T3
T2
Others
G
H
I
bodyId: 1566528972
bodyId: 1188885499
bodyId: 1566519741
J
LC11
unknown
PDL09z
others
AVL11or
PVL07w
ADL26h
PVL07oi
AVL05ol
K
AVLP
PVLP
LO
PDL09z
bodyId: 1344469820
L
AVL11or
bodyId: 1597213470
M
PVL07w
bodyId: 1374063129
N
ADL26h
bodyId: 950880008

Figure S7. Connectomic analysis of LC11 circuit, Related to Figure 4.

All data shown here is from an electron-microscopy *Drosophila* hemibrain dataset [S9]. (A) The numbers of pre- and postsynaptic terminals of LC11 neurons by brain region. LC11 mostly receives inputs from lobula (LO) and sends outputs in PVLP, where its optic glomerulus resides. LC11 also receive inputs at PVLP and sends outputs within lobula, confirming previous *syt* labeling results [S10,S11]. A small number of synapses were also identified in posterior lateral protocerebrum (PLP) and anterior ventrolateral protocerebrum (AVLP). Since the hemibrain dataset [S9] does not include the entire lobula, some instances of LC11 have a smaller number of postsynapses in lobula. (B) An example reconstructed LC11 neuron. The bar corresponding to this LC11 is marked by the black arrow in (A). "bodyId" indicates the unique identifier for this particular neuron in the hemibrain dataset [S9]. (C) The 33 putative T3 cells we identified among the presynaptic cells to the LC11 shown in (B), viewed normally. See also **Figure 4B**. (D) Same as (C), but for T2. See also **Figure 4C**. (E) Among 1,003 postsynaptic terminals of the LC11 in (B), 811 were in lobula. 495 postsynaptic terminals were connected to optic lobe-intrinsic neurons and were likely feedforward inputs. Putative T3 and T2 neurons had 137 and 38 synapses onto the LC11, respectively, which combined to account for about a third of optic lobe intrinsic inputs into the LC11. The larger number of synapses from T3 than T2 is consistent with our tGRASP results (**Figures S5B, S6B**), as well as recent optogenetic activation results [S6]. (F) Quantification of terminal morphology of presynaptic neurons to the LC11 shown in (B) by the standard deviation of presynaptic locations along the first principal component (SD_1) and the ratio between the standard deviations along the first and second principal components (SD_1/SD_2). T3 had both small SD_1 (< 4μm) and SD_1/SD_2 (< 4), reflecting its small and crumpled terminal morphology. T2 had moderate SD_1 (~ 8 μm) and large SD_1/SD_2 (> 4), reflecting its elongated shape. (G-I) Using the SD_1 and SD_1/SD_2 criteria as a guide, we identified more putative T3 and T2 cells that are presynaptic to other instances of LC11. The bars corresponding to these LC11 cells are marked by the gray, blue, and red arrows in (A). Again, T3 and T2 do not appear to localized to a specific portion of LC11 dendrites. (J) Postsynaptic targets of the LC11 neurons by the total number of synapses. LC11 has a large number of within cell type connections. Note that the cell type names are provisional (see [S9] for more details). (K-N) Examples of major postsynaptic targets of LC11, viewed from the top. PDL09z (K), AVL11or (L), and ADL26h (N) are all interneuron connecting PVLP and AVLP. (M) PVL07w receives inputs at PVLP and sends outputs back to lobula. (K) The morphology of PDL09z resembles a previously documented optic glomerulus interneuron, which is activated by small objects in a non-direction selective fashion and inhibited by turning [S12].

T3 bodyId	T3 bodyId (Contd.)	T3 bodyId (Contd.)	T2 bodyId	T2 bodyId (Contd.)
5901197093	1280617081	5812993466	1620662420	1622342905
1621682577	1714790549	1652703954	1497861652	1435468526
1434790093	1497875467	1682741229	1218888267	1714113967
1404769649	1497887946	1466489408	1589628079	1466503190
1373048670	1652038889	1620667522	1158191687	1435467893
1280293065	1621340890	1683087240	1560272804	1218887978
1807558759	1497865324	5813062188	1496859946	1373721424
1435114210	1496864079	1745488756	1188885789	1249581751
1280617267	1683078147	1589969292	1622360178	1528555578
1343377364	1683756514		1591321414	1528896615
1342371688	1558601575		1497197297	1683415341
1404428883	1435122998		1311652071	

Table S1. A list of annotated putative T3 and T2 on the hemibrain dataset, Related to Figure 4.

Supplemental References

S1. Creamer, M.S., Mano, O., and Clark, D.A. (2018). Visual Control of Walking Speed in Drosophila. Neuron *100*, 1460-1473.e6. Available at: https://doi.org/10.1016/j.neuron.2018.10.028.

S2. Zabala, F., Polidoro, P., Robie, A., Branson, K., Perona, P., and Dickinson, M.H. (2012). A simple strategy for detecting moving objects during locomotion revealed by animal-robot interactions. Curr. Biol. *22*, 1344–1350.

S3. Götz, K.G., and Wenking, H. (1973). Visual control of locomotion in the walking fruitfly Drosophila. J. Comp. Physiol. *85*, 235–266.

S4. Maimon, G., Straw, A.D., and Dickinson, M.H. (2008). A Simple Vision-Based Algorithm for Decision Making in Flying Drosophila. Curr. Biol. *18*, 464–470.

S5. Bahl, A., Ammer, G., Schilling, T., and Borst, A. (2013). Object tracking in motion-blind flies. Nat. Neurosci. *16*, 730–738. Available at: http://www.nature.com/doifinder/10.1038/nn.3386.

S6. Keleş, M.F., Hardcastle, B.J., Städele, C., Qi, X., and Frye, M.A. (2020). Inhibitory interactions and columnar inputs to an object motion detector in Drosophila. Cell Rep. *30*, 2115–2124.

S7. Manookin, M.B., Patterson, S.S., and Linehan, C.M. (2018). Neural Mechanisms Mediating Motion Sensitivity in Parasol Ganglion Cells of the Primate Retina. Neuron *97*, 1327-1340.e4. Available at: https://doi.org/10.1016/j.neuron.2018.02.006.

S8. Konstantinides, N., Kapuralin, K., Fadil, C., Barboza, L., Satija, R., and Desplan, C. (2018). Phenotypic Convergence: Distinct Transcription Factors Regulate Common Terminal Features. Cell *174*, 622-635.e13. Available at: https://doi.org/10.1016/j.cell.2018.05.021.

S9. Xu, C.S., Januszewski, M., Lu, Z., Takemura, S., Hayworth, K., Huang, G., Shinomiya, K., Maitin-Shepard, J., Ackerman, D., Berg, S., *et al.* (2020). A Connectome of the Adult Drosophila Central Brain. bioRxiv, 2020.01.21.911859.

S10. Keleş, M.F., and Frye, M.A. (2017). Object-Detecting Neurons in Drosophila. Curr. Biol., 1–8. Available at: http://linkinghub.elsevier.com/retrieve/pii/S096098221730012X.

S11. Wu, M., Nern, A., Williamson, W.R., Morimoto, M.M., Reiser, M.B., Card, G.M., and Rubin, G.M. (2016). Visual projection neurons in the Drosophila lobula link feature detection to distinct behavioral programs. Elife *5*, e21022. Available at: http://elifesciences.org/lookup/doi/10.7554/eLife.21022.

S12. Kim, A.J., Fitzgerald, J.K., and Maimon, G. (2015). Cellular evidence for efference copy in Drosophila visuomotor processing. Nat. Neurosci. *18*, 1247–1255. Available at: http://dx.doi.org/10.1038/nn.4083.